AUTHOR(S)
Xu, D., Shen, L.-L., Qin, Z.-K., Yan, S., Wang, N., Wang, J., & Gao, Y.-J.

TITLE
Construction of Reverse Type-II InP/ZnxCd1–xS Core/Shell Quantum Dots with Low Interface Strain to Enhance Photocatalytic Hydrogen Evolution

YEAR
2024

DOI
10.1021/acs.inorgchem.4c01503

CITATION
Xu, D., Shen, L.-L., Qin, Z.-K., Yan, S., Wang, N., Wang, J., & Gao, Y.-J. (2024). Construction of Reverse Type-II InP/ZnxCd1–xS Core/Shell Quantum Dots with Low Interface Strain to Enhance Photocatalytic Hydrogen Evolution. *Inorganic Chemistry*, 63(27), 12582–12592. https://doi.org/10.1021/acs.inorgchem.4c01503

VERSION
Accepted Manuscript

Construction of Reverse Type-II InP/$Zn_xCd_{1-x}S$ Core/shell Quantum Dots with Low Interface Strain to Enhance Photocatalytic Hydrogen Evolution

Dongzi Xu[1], Li-Lei Shen[1], Zhi-Kai Qin[1], Shuo Yan[1], Nianxing Wang[2], Jingui Wang[1], Yu-Ji Gao[1,]*

[1]School of Chemistry and Chemical Engineering, Faculty of Chemistry and Pharmacy, Qilu University of Technology (Shandong Academy of Science), Jinan 250353, P. R. China. [2]Department of Mechanical and Materials Engineering, University of Turku, Turku 20014, Finland. [*]Correspondence: yjgao@qlu.edu.cn

ABSTRACT: The InP-based quantum dots (QDs) have attracted much attention in the field of photocatalytic H_2 evolution. However, the shell should be used for the InP-based photocatalytic systems to passivate the numerous surface defects. Different from the traditional InP-based core/shell QDs with Type-I or Type-II band alignment, herein, the "reverse Type-II" core/shell QDs which both the conduction and valence band of shell materials are more negative than that of core materials have been well-designed by regulating the ratio of Cd/Zn of the alloyed $Zn_xCd_{1-x}S$ shell. The reverse Type-II band alignment would realize the spatial separation of photogenerated carriers. More importantly, the photogenerated holes tend to rest on the shell in the reverse Type-II QDs, which facilitates the hole transfer to the surface, the rate-determining step for solar H_2 evolution using QDs. Therefore, the obtained InP/$Zn_{0.25}Cd_{0.75}S$ core/shell QDs

exhibit superior photocatalytic activity and stability under visible light irradiation. The rate of solar H_2 evolution reaches 376.19 μmol h^{-1} mg^{-1} at initial 46 h, with the turnover number of ~2 157 000 per QD within 70 h irradiation.

KEYWORDS: InP QDs; $Zn_xCd_{1-x}S$; Photocatalytic H_2 evolution; Core/Shell QDs; Reverse Type-II heterostructure

1. INTRODUCTION

Hydrogen is considered as an ideal energy carrier for replacing the traditional fossil fuels due to its high specific enthalpy of combustion and pollution-free combustion product.[1-4] And converting solar energy into chemical energy through photocatalytic reactions and storing it in the form of H_2 is regarded as one of the most effective solutions for addressing current energy problems.[5-9] Colloidal semiconductor nanocrystals, also known as quantum dots (QDs) with the ultra-smaller size than their exciton Bohr radius, have garnered considerable attention in the realm of photocatalytic H_2 evolution.[10] Compared to bulk semiconductors, the bandgap of QDs could be tuned by adjusting their size, and the extremely small size also facilitates the exciton transfer towards the surface, thereby promoting rapid charge separation and the subsequent redox reaction.[11,12] Therefore, owing to their high light absorption coefficient, superior light harvesting capacity, large specific surface area, and abundant active sites,[13] the photocatalytic H_2 evolution reactions based on QDs have been extensively reported in recent years.

InP QDs have garnered significant attention in the photocatalytic H_2 evolution reactions because of their relatively small band gap. However, pure InP QDs are inherently susceptible to surface oxidation due to strong tetrahedral coordination from covalent bonds, resulting in their poor stability.[14,15] Additionally, there are numerous dangling bonds and defect sites on the surface of InP QDs, which makes it easy for photogenerated electrons and holes recombination. Therefore, reducing the surface defects and improving the stability is vital for their photocatalytic performance.[16,17] One strategy to address those challenges is embedding the QDs into another semiconductor material to form core/shell structured QDs. The shell would provide a physical barrier between the optically sensitive core and the surrounding medium to avoid environmental damage and photooxidation. Furthermore, the shell would also passivate the surface defects to greatly prolonging the lifetime of photogenerated electrons and holes.[18]

Haubold and co-works initially synthesized InP/ZnS core/shell nanomaterials,[19] and subsequent extensive research has shown that the ZnS shell can effectively passivate the surface defects of InP QDs and enhance their stability.[20-23] However, the lattice mismatch between InP and ZnS is as high as 7.7%, which results in the formation of interfacial defects at the core-shell interface, inducing the extra non-radiative recombination of photogenerated excitons.[24] To mitigate the lattice strain, one approach is inserting the intermediate lattice constant materials at the core-shell interface. For example, ZnSe, having a lower lattice mismatch of 3.3% with InP and 4.6% with ZnS, is utilized as a lattice buffer to enable the deposition of a thicker ZnS shell. Therefore,

the resulting InP/ZnSeS exhibit superior optical property and stability. [25,26] However, the strain at the core-shell interface would enlarge with increasing shell thickness.[27] An alternative to reduce interfacial strain is to adjust the lattice constant of core or shell, especially when using solid solutions as the core or shell materials.[28] By doping the Zn^{2+} into the InP QDs, the lattice constants reduces from 0.593 nm for InP to 0.539 nm for the obtained In_xZn_yP alloy, which ensures the epitaxial growth of $ZnSe_zS_{1-z}$ shells with minimum lattice mismatch and results in the maximum photoluminescence (PL) quantum yield.[29] Studies also reveal that the interface strain of the InP core with shell would shift from compression to tension with increasing the ration of CdSe to ZnSe in the InP/(Zn, Cd)Se core/shell QDs. [28,30]

Apart from the interface strain, the band alignment of the core and shell in core/shell QDs also affects the photocatalytic performance. Generally, the core/shell QDs are classified into Type-I, reverse Type-I, and Type-II configurations based on the relative positions of conduction band (CB) and valance band (VB) between core and shell.[18] In Type-I core/shell QDs, the CB of the shell is more negative than that of the core, while the VB of the shell is more positive than that of the core. Therefore, both the photogenerated electrons and holes are confined within the core QDs. The shell would serve as the tunneling barrier for the electron and hole transfer to the surface and slow down their rates,[31] which is unfavorable for the photocatalytic H_2 evolution. Owing to the broad band gap of ZnS, the InP/ZnS is a typical Type-I core/shell QDs. However, to improve the migration efficiency of electrons and holes, the Cu^{2+} is doped into the

ZnS shell to decrease the band gap of the shell, thereby enhances their photocatalytic H_2 evolution activity.[22]

Among them, the Type-II core/shell QDs exhibits greater advantages in photocatalytic H_2 evolution owing that both the CB and VB of the core are more positive (or more negative) than that of the shell, therefore only one type of carrier is mostly delocalized from the absorber materials to the other materials of QDs, realizing the spatial separation of photogenerated electrons and holes. For example, in the Type-II InP/ZnO core/shell QDs, both the CB and VB of the shell are more positive than that of the core. Therefore, the photogenerated electrons would delocalize into the shell while the holes remain in the core.[32] However, the holes transfer and the subsequent redox reaction is usually the rate-determining step for QDs-based photocatalytic H_2 evolution.[33] And the confined holes in the core is unfavorable for the improvement of the overall photocatalytic H_2 evolution activity. Specially, the Type-II core/shell QDs are also divided into traditional Type-II and reverse Type-II heterostructure QDs to further highlight the advantage of the latter.[34] For the reverse Type-II core/shell QDs, the CB and VB of the core are more negative than that of the shell. So the holes are usually located in the shell after irradiation, which is conducive for the hole transfer to the QDs surface and the subsequent reaction with electron donor.

$Zn_xCd_{1-x}S$ alloy have been widely studied because it has the advantages of both ZnS and CdS.[35-37] ZnS could improve the photostability of CdS and enhances the separation efficiency of electrons and holes, while CdS with the narrower bandgap can enhance the visible light absorption capacity of ZnS. Moreover, the lattice mismatch between

InP (0.587 nm) and CdS (0.583 nm) is only 0.7%, which is significantly smaller than that of ZnS (7.7%).[38] Herein, the InP QDs are used to serve as the core and the $Zn_xCd_{1-x}S$ alloys are epitaxially deposited on their surface to constructure the core/shell QDs. The $Zn_xCd_{1-x}S$ could not only passivate the InP core but also mediate the interfacial lattice strain by the alloyed shell. In addition, the reverse Type-II heterostructure QDs are also obtained by regulating the ratio of Cd/Zn, which is beneficial to the separation of photogenerated charges and the holes transfer to the surface of QDs, thereby improving their photocatalytic performance. Under optimal conditions, the InP/$Zn_{0.25}Cd_{0.75}S$ core/shell QDs displayed an exceptional H_2 evolution rate of ~376.19 μmol h^{-1} mg^{-1} at initial 46 h, giving the turnover number (TON) of ~2 157 000 per QD within 70 h irradiation.

2. EXPERIMENTAL SECTIONS

No uncommon hazards are noted.

Materials. Indium chloride tetrahydrate ($InCl_3 \cdot 4H_2O$, 99.99%), zinc chloride ($ZnCl_2$, 98%), sulfur (S, 99.99%), cadmium oxide (CdO, 99%) and zinc acetate dihydrate ($Zn(CH_3COO)_2 \cdot 2H_2O$) were purchased from Macklin. Nickel acetate tetrahydrate ($Ni(CH_3COO)_2 \cdot 4H_2O$, 99%), oleylamine (OAm, 95%), tris (dimethylamine) phosphorus ($(DMA)_3P$, 98%), 1-octadecene (ODE, 90%), oleic acid (OA, 90%) and 3-mercaptopropionic acid (3-MPA, 99%) were purchased from 3A Materials. Other chemicals were of analytical grade and all reagents were used directly without further purification. Ultrapure water with 18.2 MΩ·cm was used throughout the experiments.

Synthesis of InP QDs. The InP QDs were synthesized by the hot injection method. Generally, 0.34 mmol of $InCl_3 \cdot 4H_2O$, 2.2 mmol of $ZnCl_2$ and 5 mL of OAm were added to the three-necked flask. The solution was heated under an argon atmosphere to 140 ℃ for 1 h to mix the solution evenly, and then the temperature was raised to 200 ℃. At this time, the mixture of $(DMA)_3P$ and OAm (2.4 mmol of $(DMA)_3P$ dissolved in 1 mL of OAm) was quickly injected. After the growth of InP QDs at 200 ℃ for 20 mins, the solution was quickly cooled to room temperature. The QDs were purified with anhydrous ethanol and then stored in a 10 mL n-hexane solution. The concentration of InP QDs was calculated based on the UV-vis to be 0.274 μmol mL^{-1}.[21]

Synthesis of InP/$Zn_xCd_{1-x}S$ QDs. A cadmium precursor solution (Cd-OA, 0.2 mol/L) was prepared by dissolving 260 mg of CdO in 3 mL of OA and 7 mL of ODE at 280 °C. A zinc precursor solution (Zn-OA, 0.2 mol/L) was prepared by dissolving 440 mg of $Zn(CH_3COO)_2 \cdot 2H_2O$ in 4 mL of OA and 6 mL of ODE at 240 °C. Both the Cd-OA and Zn-OA precursor solution was maintained at 90 °C after complete dissolution. A sulfur precursor solution (0.2 mol/L) was prepared by dissolving 64 mg of sulfur in 10 mL of ODE at 130 °C and then maintained at room temperature.

The InP/$Zn_xCd_{1-x}S$ core-shell QDs were synthesized by the successive ionic layer adsorption and reaction (SILAR) method.[39] Generally, 0.5 μmol of InP QDs, 5 mL of ODE and 5 mL of OAm were added to 100 mL three-necked flask. The n-hexane was removed by vacuumizing after heating. Then the temperature raised to 150 °C and the calculated amounts of Cd-OA and Zn-OA precursor solution were injected into the system and the temperature was immediately raised to 240 ℃. After 5 mins, the

calculated amounts of S-ODE were slowly injected into the system to grow the first monolayer for 20 mins. All subsequent precursor solutions were alternately added at 240 ℃ by the same steps to grow a thicker shell. The obtained core/shell QDs were purified with anhydrous ethanol and finally stored in a 10 mL n-hexane solution. Simultaneously, the $Zn_xCd_{1-x}S$ QDs were also synthesized according to the previously reported method for comparison.[40]

Ligand Exchange. The prepared QDs were transferred into an aqueous solution through ligand exchange protocol before photocatalytic experiments. First, 1.0 mL of the above QDs/n-hexane solution was added in a 10 mL centrifuge tube. And then 5 mg of NaOH particles and 30 μL of 3-MPA were added. After stirring for about 10 mins, the mixture was centrifugated at 8000 rpm for 5 mins. The precipitation was washed with n-hexane and water/acetone, respectively. After centrifuging, the obtained precipitate was dispersed in 1.0 mL of water.

Photocatalytic H_2 Evolution. In generally, 0.2 mL of aqueous QDs solution, 1.0 mL of IPA, 0.2 mL of saturated NaOH solution, 0.01 mg of $Ni(CH_3COO)_2 \cdot 4H_2O$ and ultra-pure water were added to a Pyrex tube. The total volume of the mixture was 6.0 mL. The Pyrex tube was de-aerated by bubbling Ar for 10 min to remove residual air. And then 1.0 mL of CH_4 gas was injected as an internal standard for gas chromatography (GC) analysis. The photocatalytic H_2 evolution experiment was carried out under the 420 nm light-emitting diodes (LEDs, 100 mW cm^{-2}) irradiation and the amount of produced H_2 gas was measured by GC.

3. RESULT AND DISCUSSION

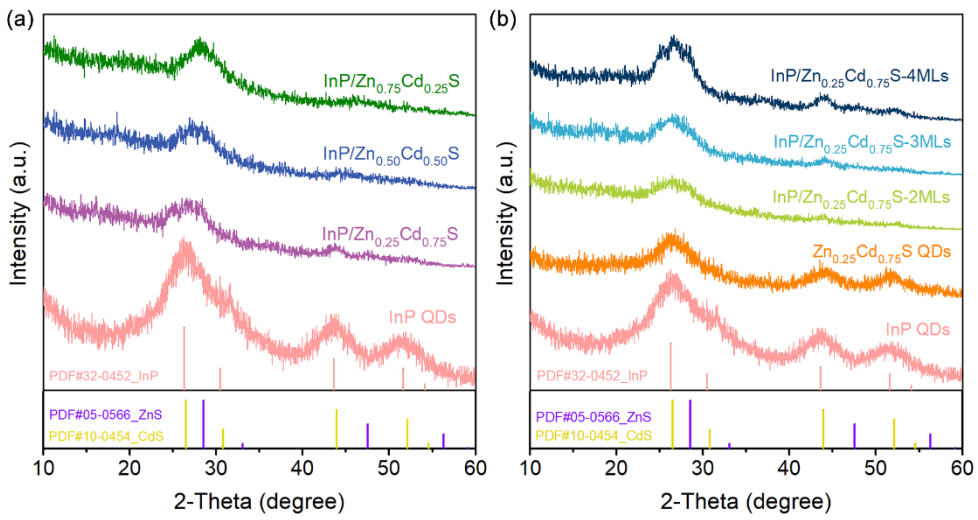

Figure 1. (a) The XRD of InP/$Zn_xCd_{1-x}S$ with different ratio of Cd/Zn. (b) The XRD of InP QDs, $Zn_{0.25}Cd_{0.75}S$ QDs, and InP/$Zn_{0.25}Cd_{0.75}S$ core/shell QDs with different shell thickness.

Here, the InP core QDs were synthesized via a hot-injection method. And then $Zn_xCd_{1-x}S$ alloy shell were epitaxially grown on the surface of InP QDs through the modified SILAR method in organic solution. The core/shell QDs with different ratio of Cd/Zn were obtained by regulating the ratio of Cd and Zn precursor, while the InP/$Zn_{0.25}Cd_{0.75}S$ core/shell QDs with different shell thickness were synthesized by regulating the precursor amount and using the theoretical monolayers (MLs) to distinguish. Firstly, the crystalline structure of various InP and InP/$Zn_xCd_{1-x}S$ QDs was analyzed by X-ray diffraction (XRD). As shown in Figure 1a, the InP QDs exhibited three characteristic diffraction peaks at 2θ values of 26.30°, 43.60°, and 53.60°, which is corresponding to the (111), (220), and (311) planes of InP (JCPDS card No. 32-0452), respectively, indicating the zinc blende structure. It can be clearly observed from Figure S1 that the diffraction peaks of the (111), (220) and (311) planes belonging to the cubic

crystal $Zn_xCd_{1-x}S$, indicating that the shell layer is a cubic crystal structure.[41] The diffraction peaks of the core/shell QDs systematically shifted towards lower angles with the increased ratio of Cd/Zn, indicating that the shell of InP/$Zn_xCd_{1-x}S$ is an alloyed semiconductor.[42] Moreover, the lower-angle shift of the core/shell QDs with the increased content of Cd demonstrated the lattice expansion of QDs. At Cd content of 75%, the diffraction peaks of the core/shell QDs approached those of the InP core, indicating that the lattice mismatch between the shell and InP is smaller, as well as the low interface strain between the core and shell. In order to further prove the low interfacial strain between the core and the shell, the lattice constants were calculated through the XRD of InP QDs (Figure 1) and pure $Zn_xCd_{1-x}S$ QDs (Figure S1, see the detailed calculation process in Supporting Information). The lattice constant of the InP QDs and $Zn_{0.75}Cd_{0.25}S$, $Zn_{0.50}Cd_{0.50}S$, $Zn_{0.25}Cd_{0.75}S$ are 5.87 Å, 5.54 Å, 5.69 Å and 5.80 Å, respectively. It intuitively indicates that the lattice mismatch for the $Zn_{0.25}Cd_{0.75}S$ with InP is lower than the other $Zn_xCd_{1-x}S$ nanocrystals, demonstrating the low interface strain at the InP/$Zn_{0.25}Cd_{0.75}S$ QDs. Upon fixing the Zn:Cd ratio and increasing the shell thickness, the diffraction peak width of InP/$Zn_xCd_{1-x}S$ core/shell QDs narrowed as the shell grew thicker (Figure 1b). The narrowed diffraction peaks implied the increased diameter of the core/shell QDs according to the Scherrer formula. This initially proves the successful synthesis of InP/$Zn_xCd_{1-x}S$ core/shell QDs with different shell thickness.

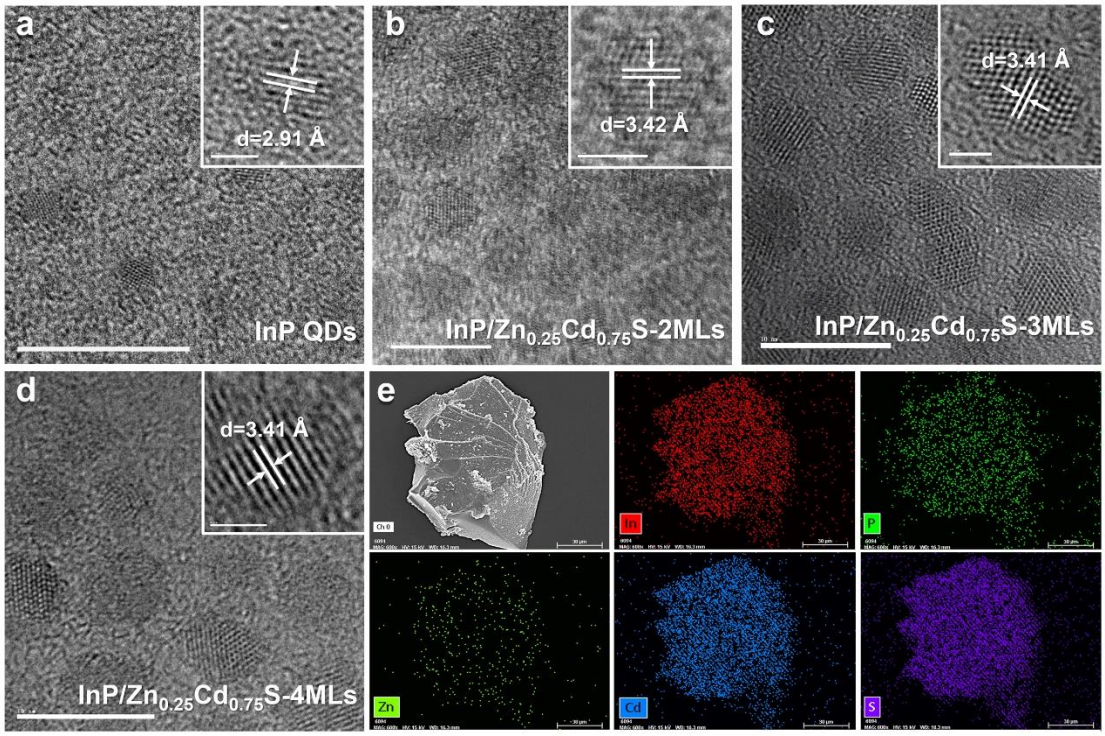

Figure 2. (a) The TEM image of InP QDs. (b-d) The TEM image of InP/$Zn_{0.25}Cd_{0.75}S$ with different shell thickness. (e) The EDS of InP/$Zn_{0.25}Cd_{0.75}S$-3MLs. The inset figures in a-d exhibit the HR-TEM images and their corresponding lattice spacing, respectively. All scale bar of a-d is 10 nm, and the scale bar of illustrations is 2 nm.

The morphology of InP QDs and various InP/$Zn_{0.25}Cd_{0.75}S$ core/shell QDs with different shell thickness was analyzed by transmission electron microscopy (TEM). Figure 2a shows that the InP QDs are spherical ultra-small nanocrystals with the diameter of ~2.83 nm. The high-resolution TEM (HR-TEM) image reveals a lattice spacing of 2.91 Å, which is corresponding to the (200) plane of zinc blende InP. After the epitaxial growth of the alloy shell, the size of obtained core/shell QDs increases obviously. The diameter of InP/$Zn_{0.25}Cd_{0.75}S$ QDs for 2 MLs, 3 MLs, and 4 MLs are ~4.12 nm, ~4.93 nm, and ~5.56 nm, respectively, following the expected trend with a shell thickness per monolayer (0.31 nm for ZnS monolayer and 0.35 nm for CdS

monolayer) (Figures 2b-d). It clearly demonstrates the successful synthesis of InP/$Zn_{0.25}Cd_{0.75}S$ QDs with varied shell thicknesses. When the ratio of Zn increases to 50% and 75%, the morphology of the core-shell QDs becomes confused (Figures S2b-d). This is attributed to the large lattice mismatch between ZnS and InP, and the larger content of ZnS would result in the higher lattice strain and massive defects at the core/shell interface.[43] The lower lattice mismatch of 0.7% between CdS and InP largely could mitigate lattice strain effects,[44] facilitating a more uniform shell growth, leading to InP/$Zn_{0.25}Cd_{0.75}S$ QDs with an approximate spherical configuration. In addition, the observed lattice spacing of the cubic InP/$Zn_{0.25}Cd_{0.75}S$ QDs is ~3.41 Å (Figures 2b-d), which is attributed to the (111) plane of cubic $Zn_{0.25}Cd_{0.75}S$ shell. The lattice spacing is very close to the (111) plane of cubic InP (3.89 Å, JCPDS card No. 32-0452), implying the lower interface strain between the core and shell. Hereafter, the core/shell QDs of InP/$Zn_{0.25}Cd_{0.75}S$ prepared with 25% Zn and 75% Cd is denoted as InP/ZCS.

In order to demonstrate the elemental composition in the core/shell QDs, the macroscopic element mapping of the InP/ZCS QDs was performed by scanning electron microscopy (SEM) coupled with energy-dispersive X-ray spectroscopy (EDS). Figure 2e presents the EDS element mapping of InP/ZCS-3MLs and although the accurately position of each element in a single QD cannot be provided, the macroscopically homogeneous distribution of In, P, Zn, Cd, and S elements implies the coexistence of all the elements in the QDs. In addition, the EDS quantitative analysis indicates that the atomic ratio of Cd to Zn in InP/$Zn_{0.25}Cd_{0.75}S$ core/shell QDs is close to 3:1 (Table S1). The accurate atomic ratio in the InP/$Zn_{0.25}Cd_{0.75}S$-3MLs was also

determined by the inductively coupled plasma mass spectrometry (ICP-MS). As shown in Table S2, the normalized atomic contents of Zn and Cd are 6.90% and 24.10%, respectively, giving the mole ratio of 0.22:0.78 for Zn to Cd, which is very close to the stoichiometry in the synthesis process.

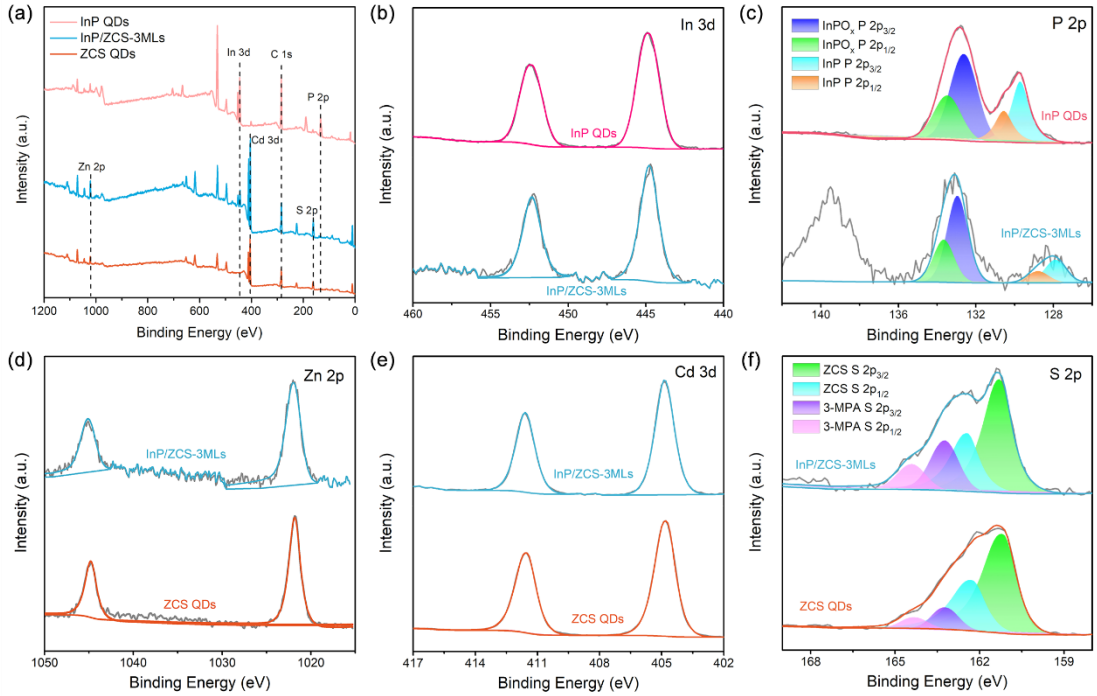

Figure 3. (a) The XPS survey of InP QDs, InP/ZCS-3MLs QDs, and $Zn_{0.25}Cd_{0.75}S$ (ZCS) QDs. The high-resolution XPS spectra of In 3d (b) and P 2p (c) for InP QDs and InP/ZCS-3MLs. The high-resolution XPS spectra of Zn 2p (d), Cd 3d (e), and S 2p (f) for InP/ZCS-3MLs and ZCS QDs.

Subsequently, the X-ray photoelectron spectroscopy (XPS) is used to further analyze the elemental composition and chemical environment of various QDs. In Figure 3a, the XPS survey of InP/$Zn_{0.25}Cd_{0.75}S$-3MLs exhibits clearly signals corresponding to In 3d, P 2p, Zn 2p, Cd 3d, and S 2p, consistent with the result in SEM-EDS (Figure 2e) and ICP-MS (Table S2). And the similar signals are also detected in the InP/$Zn_xCd_{1-x}S$

core/shell QDs with different ratio of Cd/Zn, indicating the reasonable element composition of synthesized QDs (Figure S3). The characteristic peaks of In 3d are located at 444.8 eV and 452.4 eV (Figure 3b), which are characteristic of In $3d_{5/2}$ and In $3d_{3/2}$ states in In^{3+}, respectively.[45] Deconvolution of the core/shell quantum dots (Figure 3c) reveals two pairs of P states, the one at 129.95 eV and 130.85 eV is attributed to the P $2p_{3/2}$ and $2p_{1/2}$ levels in InP QDs, while the another at 133.04 eV and 133.94 eV is attributed to the P $2p_{3/2}$ and $2p_{1/2}$ in $InPO_x$, originating from the surface oxidation of InP.[46] Compared with InP QDs, the P 2p binding energy in InP/ZCS-3MLs shifts slightly towards lower energies, which is attributed to the increased electronic states of P atoms interacting with metal atoms on the shell layer.[47] Notably, a new peak appears at 139 eV in InP/ZCS-3MLs, which can be attributed to the Zn 3s peak. The Zn 2p spectrum of Zn^{2+} displays peaks at binding energies of 1045.1 eV and 1022.0 eV for Zn $2p_{1/2}$ and Zn $2p_{3/2}$, respectively (Figure 3d).[48] Compared with the ZCS QDs, the Zn 2p binding energy of InP/ZCS-3MLs slightly shifts to higher energy, which is in concert with the low-energy shift of P 2p, indicating the formation of P-Zn bonds at the core-shell interface.[47] The presence of Cd^{2+} is demonstrated by the peaks at 404.8 eV and 411.6 eV (Figure 3e), corresponding to Cd $3d_{5/2}$ and Cd $3d_{3/2}$, respectively.[49] It is worth noticing that two pairs of S 2p peaks are observed in Figure 3f. The peaks at 161.3 eV and 162.5 eV belong to the S 2p of metal sulfide in the ZCS shell.[40] While the peaks at 163.3 eV and 164.5 eV are attributed to the S in the organic ligand of 3-MPA on the surface of the QDs after ligand exchange,[46] which also have been observed by ICP-MS for the excess S (Table S2). This highlights the detailed chemical

information regarding the interaction of the various components within the $InP/Zn_{0.25}Cd_{0.75}S$ core/shell QDs.

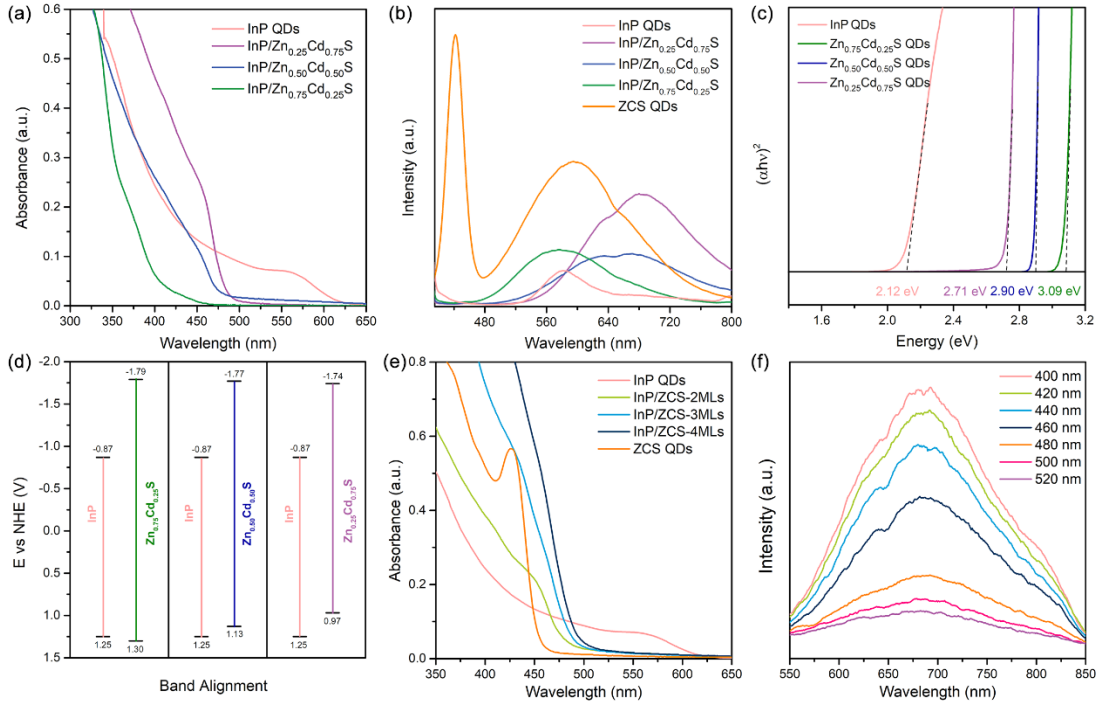

Figure 4. (a) UV-vis absorption spectra of InP QDs and $InP/Zn_xCd_{1-x}S$-2MLs core/shell QDs with different ratio of Cd/Zn. (b) Photoluminescence spectra of InP QDs, ZCS QDs and $InP/Zn_xCd_{1-x}S$-2MLs core/shell QDs with different ratio of Cd/Zn, excitation wavelength: 400 nm. (c) Tauc plots of InP QDs and $Zn_xCd_{1-x}S$ QDs with different ratio of Cd/Zn. (d) The band alignment of $InP/Zn_xCd_{1-x}S$ QDs with different ratio of Cd/Zn. (e) UV-vis absorption spectra of InP QDs, ZCS QDs and InP/ZCS with different shell thickness. (f) Photoluminescence spectra of $InP/Zn_{0.25}Cd_{0.75}S$-2MLs excited by different light.

Steady-state UV-vis absorption and photoluminescence spectra were employed to investigate the pathways of photogenerated electron transfer in the core-shell quantum dots. As depicted in Figure 4a, the first absorption peak of InP is observed at 550 nm,

indicating that the obtained InP is an ultra-small nanocrystal with the quantum confinement effects.[50] Following the deposition of the shell, the absorption peak of core/shell QDs blue-shifts significantly, which could be attributed to the transition of the dominant absorption from InP to the thick shell (Figure 4a).[44] And the absorption of InP in the core/shell QDs is almost disappeared (Figure S4), which is owing that the ratio of the InP core is very small in the obtained InP/ZCS QDs, as well as the coverage of the shell would spread the wave function of core to reduce wave function overlap between the carriers.[46] Compared with the significant blue-shift of the absorption spectra, no such blue-shift is observed in the emission peak. As shown in Figure 4b, InP QDs exhibit a weak emission peak at 577 nm, which is attributed to the bandgap emission of InP QDs. While the ZCS QDs exhibit two emission peaks, the strong bandgap emission at 440 nm and broad defect emission at 600 nm. After coating with the $Zn_{0.75}Cd_{0.25}S$ shell, the emission wavelength of obtained core/shell QDs is similar to that of InP QDs, suggesting the Type-I heterostructure of InP/$Zn_{0.75}Cd_{0.25}S$ core/shell QDs. With increasing the Cd content in the shell, the emission peaks for core/shell QDs with $Zn_{0.50}Cd_{0.50}S$ and $Zn_{0.25}Cd_{0.75}S$ shells red-shift obviously, implying a change in the heterojunction type of the obtained core/shell QDs.

Therefore, Tauc plots (Figure 4c) from the UV-vis spectra (Figure S5) and valence band XPS spectra (Figure S6) were used to characterize the bandgaps and band alignments of InP/$Zn_xCd_{1-x}S$ with different Cd/Zn ratio. As shown in Figure 4d, for InP/$Zn_{0.75}Cd_{0.25}S$ core/shell QDs, the CB and VBM of the shell are more negative and positive than those of the InP core, respectively, giving the Type-I band alignment.

With the increase of Cd content in the $Zn_xCd_{1-x}S$ alloy shell, the bandgap and VB gradually decrease while the CB becomes more positive.[51] Thus, when the Cd ratio is ≥50%, both the CB and VB of the InP core are positive than those of the shell, suggesting the reverse Type-II structure of the resulted InP/$Zn_xCd_{1-x}S$ core/shell QDs.[34] Upon photoexcitation, the shell dominantly absorbs light to produce photogenerated electrons and holes. And then, the photogenerated electrons delocalize from the CB of the shell to the CB of the InP core, while the photogenerated holes remain in the VB of the shell. The photogenerated electrons transferred to the core can radiative recombine with the photogenerated holes on the shell and emit fluorescence. In addition, for InP/$Zn_{0.25}Cd_{0.75}S$ QDs, the potential difference between the CB of the core and the VB of the shell is 1.84 eV, which is close to the energy of the PL at 680 nm, offering additional evidence for this process.

On the other hand, the PL intensity of InP/$Zn_{0.25}Cd_{0.75}S$ is significantly higher than that of InP/$Zn_{0.75}Cd_{0.25}S$ and other core/shell QDs, indicating that there are less interfacial defects. Which also implied that high content of Cd could reduce the interface strain and lattice mismatch between the core and shell.[29] As the shell thickness increases, the absorption peak red-shifts slightly (Figure 4e), which can be attributed to the weakening of quantum confinement effects in the shell due to increased shell thickness. Nevertheless, the fluorescence emission peak wavelength of the core/shell QDs has hardly changed (Figure S7), possibly because the quantum confinement effect predominantly affects the CB of semiconductors, exerting a weaker influence on the VB.[52]

Figure 4f exhibits the PL spectra of InP/$Zn_{0.25}Cd_{0.75}S$-2MLs under different excitation wavelengths. The absorption wavelengths of bare $Zn_{0.25}Cd_{0.75}S$ QDs are mainly in the range of less than 460 nm (Figure 4e). As the excitation wavelength for InP/$Zn_{0.25}Cd_{0.75}S$-2MLs QDs increases, the emission intensity decreases gradually, aligning with the variation trend of the light absorption capability. However, the emission intensity decreased significantly when the excitation wavelength was changed from 460 nm to 480 nm. With the further increase of the excitation wavelength, the decreasing trend of emission intensity becomes smaller again. The reason behind this behavior is that when the excitation wavelength is less than 460 nm, both the InP core and the ZCS shell are excited, while the absorption of ZCS shell is predominant. When the excitation wavelength exceeds 480 nm, the energy of the incident light is insufficient to excite the shell, so only InP core can be excited. In this case, photogenerated electrons remain in the CB of the InP core, but the photogenerated holes delocalize into the VB of the shell. Therefore, its PL still represents the radiative recombination of photogenerated excitons from the CB of the InP core to the VB of the $Zn_{0.25}Cd_{0.75}S$ shell, retaining the Type-II emission characteristics.

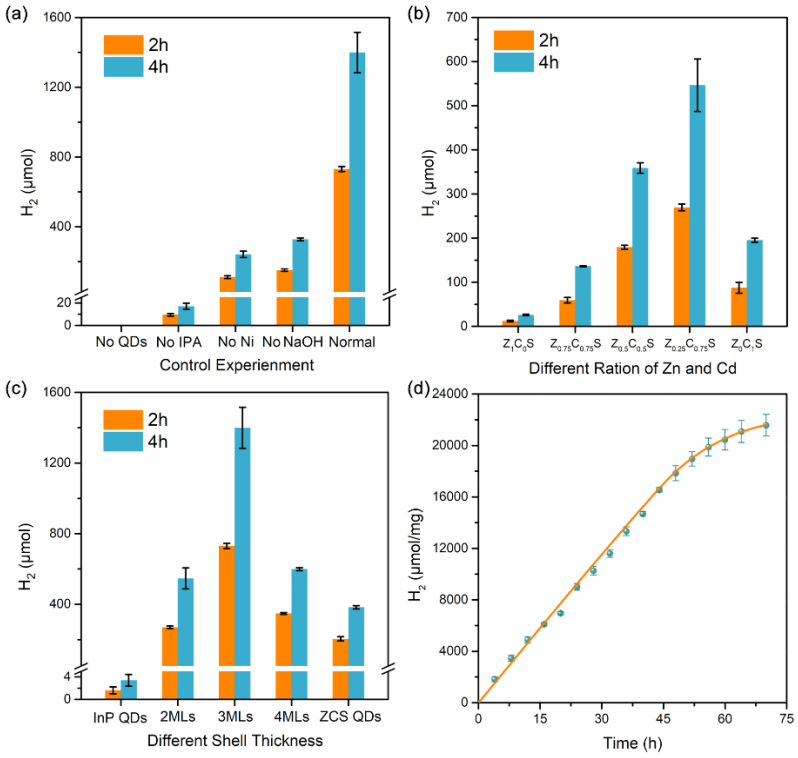

Figure 5. (a) Comparison of photocatalytic H_2 evolution for InP/ZCS-3MLs QDs without photocatalysts, IPA, Ni^{2+} cocatalysts, highly alkaline condition, and the normal condition, respectively. (b) Photocatalytic H_2 evolution experiments of InP/$Zn_xCd_{1-x}S$-2MLs with different ratio of Cd/Zn, from left to right: InP/ZnS, InP/$Zn_{0.75}Cd_{0.25}S$, InP/$Zn_{0.50}Cd_{0.50}S$, InP/$Zn_{0.25}Cd_{0.75}S$, and InP/CdS under the identical conditions. (c) Photocatalytic H_2 evolution experiments of InP QDs, InP/ $Zn_{0.25}Cd_{0.75}S$ core/shell QDs with different shell thickness, and ZCS QDs. (d) Long-time photocatalytic H_2 evolution of InP/ZCS-3MLs under the optimal conditions. Error bars represent ±s.d. of multiple independent experiments.

H_2 evolution experiments were performed to evaluate the potential photocatalytic applications of the InP/ZCS core/shell QDs. Firstly, the control experiments were performed to evaluate the synergistic effect among the QDs photocatalysts, Ni

cocatalysts, electron donor and the highly alkaline condition. As shown in Figure 5a, no H_2 is produced when there is no photocatalysts, InP/ZCS-3MLs QDs. Without the IPA, only a small amount of H_2 is separated out, which is owing that the surface organic ligands, 3-MPA, serve as the electron donor.[53,54] Without the inorganic Ni ions, it could produce H_2 with the relatively frail rate, implying the vital roles of the H_2 evolution cocatalysts. Without adding NaOH, the photocatalytic activity of the system is also very low. According to the previous report, the hydroxyl anion/radical redox couple could be produced under highly alkaline conditions, which would serve as a redox shuttle to efficiently transmit the photogenerated hole from the semiconductor to electron donor, resulting in the substantial enhancement of photocatalytic activity.[55] With the assistance of cocatalysts and highly alkaline conditions, ~1400 μmol of H_2 was produced under 4 h irradiation for the InP/ZCS-3MLs, 82.4, 5.8 and 4.3 times higher than the original absent conditions, respectively.

Subsequently, the influence of varying Zn-to-Cd ratio in the shell on photocatalytic performance of the core/shell QDs was investigated (Figure 5b). When the shell was pure ZnS, the H_2 evolution was just 25.98 μmol within 4 h irradiation, probably owing to faint absorption capacity and the increased non-radiative recombination at the core/shell interface defects caused by the substantial lattice mismatch between ZnS shell and InP core. However, with the increase of Cd/Zn ratio of the alloy $Zn_xCd_{1-x}S$ shell, the photocatalytic activity of InP/ZCS-2MLs core/shell QDs improved significantly, giving the optimal Cd/Zn ratio of 3:1, which is 21.0 times higher than that of pure ZnS shell. While the further increase of Cd contents, the pure CdS shell, the

photocatalytic activity of the obtained core/shell QDs declined. The change trend of the photocatalytic activity with the increased Cd-to-Zn ratio is consistent with that of pure $Zn_xCd_{1-x}S$ nanoparticles.[56]

Figure 5c reveals the effect of different shell thickness on photocatalytic H_2 evolution activity for InP/$Zn_{0.25}Cd_{0.75}S$ core/shell QDs. Only a trace amount of H_2 gas, 3.4 μmol, was produced for bare InP QDs within 4 h reaction. After the modification of $Zn_{0.25}Cd_{0.75}S$ shell, the photocatalytic activity of the core/shell QDs increased obviously with the increased thickness and reached the maximum for the 3 monolayers shell coverage. And then the H_2 evolution activity declined with the further increase of shell thickness, probably owing that the excessive thick shell would block the photogenerated excitons transfer from the InP core to the surface of core/shell QDs.[57] However, the activity of InP/ZCS QDs is still higher than that of pure $Zn_{0.25}Cd_{0.75}S$ QDs, implying the fantastic superiority of core/shell QDs in the field of photocatalytic H_2 evolution.

Following these optimizations, long-time photocatalytic H_2 evolution experiment of the InP/$Zn_{0.25}Cd_{0.75}S$-3MLs was conducted by using the Ni^{2+} as cocatalysts, IPA as electron donor, and under highly alkaline condition. Moreover, 0.5 mL of IPA and 0.1 mL of saturated NaOH was added every 10 hours to replenish the consumed electron donor. Figure 5d reveals that the InP/ZCS-3MLs QDs maintain a robust photocatalytic H_2 evolution for the initial 46 h, giving the nearly constant rate of 376.19 μmol h^{-1} mg^{-1}. To our best knowledge, the value is in the top-performing of photocatalytic H_2 evolution systems (Table S3). Moreover, the apparent quantum yield (AQY) of the

InP/ZCS-3MLs QDs could reach to 23.72 % at 420 nm (see details in the Supporting Information). Subsequently, the H_2 evolution rate gradually dropped. The diffraction peaks intensity of the InP/$Zn_{0.25}Cd_{0.75}S$-3MLs QDs decrease significantly after long-time irradiation (Figure S8), and the decreased crystallinity of the photocatalysts implies the photocorrosion of InP/$Zn_{0.25}Cd_{0.75}S$-3MLs QDs after long-time photocatalytic reactions. However, the addition of Zn enhances the photostability of InP/ZCS-3MLs compare with InP/CdS-3MLs, which the linear photocatalytic H_2 evolutions for InP/CdS-3MLs is 34 h (Figure S9). About 483.2 mL of H_2 gas was produced from a 6.0 mL of photocatalytic system within 70 h irradiation, giving the TON of ~2 157 000 with respect to the InP/ZCS-3MLs QDs.

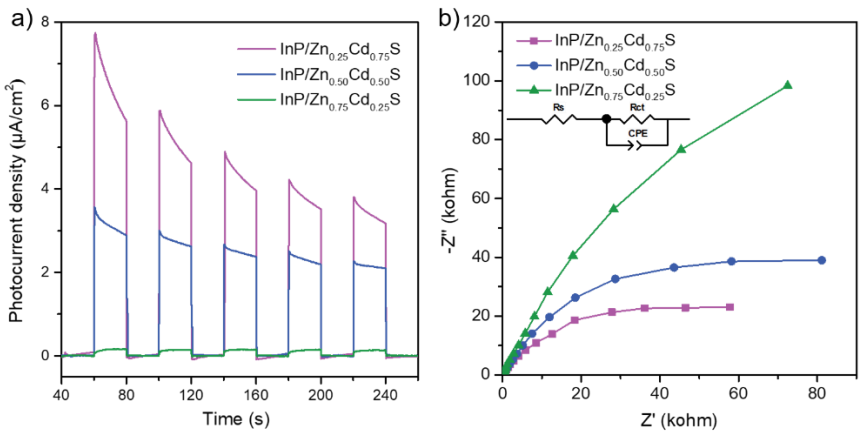

Figure 6. (a) Transient photocurrent responses to on-off irradiation and (b) electrochemical impedance test of InP/$Zn_xCd_{1-x}S$ with different ratio of Cd/Zn.

To further investigate the separation and transfer of photogenerated carriers, transient photocurrent responses were performed for several switching cycles under the same irradiation conditions, along with electrochemical impedance spectroscopy tests. The photocurrent intensity of InP/$Zn_xCd_{1-x}S$ QDs increased with rising Cd content of the

shell, and the InP/$Zn_{0.25}Cd_{0.75}S$ exhibited the highest photocurrent intensity (Figure 6a), indicating that more electrons were transported to the QDs surface. On the other hand, the radius of the high-frequency arc in the Nyquist plots obtained from electrochemical impedance testing also decreased as the Cd content increased, the fitted R_{ct} value for InP/$Zn_{0.25}Cd_{0.75}S$ is evaluated as 76.21 kΩ, which is remarkably lower than that of InP/$Zn_{0.50}Cd_{0.50}S$ (151.06 kΩ) and InP/$Zn_{0.75}Cd_{0.25}S$ (441.64 kΩ), implying that the strain-induced resistance to electron transfer was reduced for InP/$Zn_{0.25}Cd_{0.75}S$ QDs (Figure 6b). This is also consistent with the previous H_2 evolution experiments (Figure 5b). By optimizing the shell thickness, InP/ZCS-3MLs showed the highest photocurrent intensity and smaller charge transfer resistance (Figures S10a-b), signifying that the shell thickness of three monolayers offered the highest efficiency in photogenerated charge carrier separation and transfer.[58] For bare InP, the photocurrent intensity was nearly zero (Figure S10a), evidencing the effective passivation and protection provided by the shell layer.

Based on the above results, the motive and mechanism of the superior photocatalytic H_2 evolution performance for InP/ZCS-3MLs core/shell QDs are proposed. In the InP/$Zn_xCd_{1-x}S$ QDs, the introduction of the alloyed shell would passivate the surface defects of InP. And by increasing the Cd/Zn ratio of the shell, the interfacial strain between the core and shell would reduce, which further minimize the lattice mismatch and the interface defects. Moreover, the absorption of the InP/ZCS-3MLs QDs is dominated by the ZCS shell, which significantly enhances the light absorption capability of the QDs photocatalysts. On the other hand, with the increase of Cd contents in the alloy shell,

the band alignment of obtained core/shell QDs changes from Type-I for InP/$Zn_{0.75}Cd_{0.25}S$ to reverse Type-II for InP/$Zn_{0.25}Cd_{0.75}S$. The reverse Type-II band alignment would cause the photogenerated electrons delocalization from the CB of the shell to the CB of core, while the photogenerated holes still confine in the VB of shell. The spatially separated electron-hole pairs would suppress the backward recombination of photogenerated carriers, increasing the efficiency of photogenerated excitons participating in the reaction. More importantly, the holes transfer and the subsequent redox reaction is usually the rate-determining step for photocatalytic H_2 evolution.[59] However, the confined holes in the shell is conducive to the hole transfer to the surface of core/shell QDs. And the highly alkaline conditions will produce the hydroxyl anion/radical redox couple, which also greatly accelerates the oxidation section of the photocatalytic systems.

Figure 7 unravels the process of photocatalytic H_2 evolution for InP/$Zn_{0.25}Cd_{0.75}S$ core/shell QDs. The electrons and holes are generated mainly in the shell under visible light irradiation. Owing to the reverse Type-II band alignment, the photogenerated electrons rapidly delocalizes to the InP core while the holes still confine in the alloy shell, and the spatial separation would suppress the backward recombination of photogenerated carriers. And then, the holes facilely deliver to the surface of core/shell QDs and rapidly oxidize electron donor with the assistant of hydroxyl anion/radical redox couple. While the photogenerated electrons in the core are easier to tunnel to the surface of core/shell QDs and realize the proton reduction into molecular H_2 at the Ni cocatalysts.

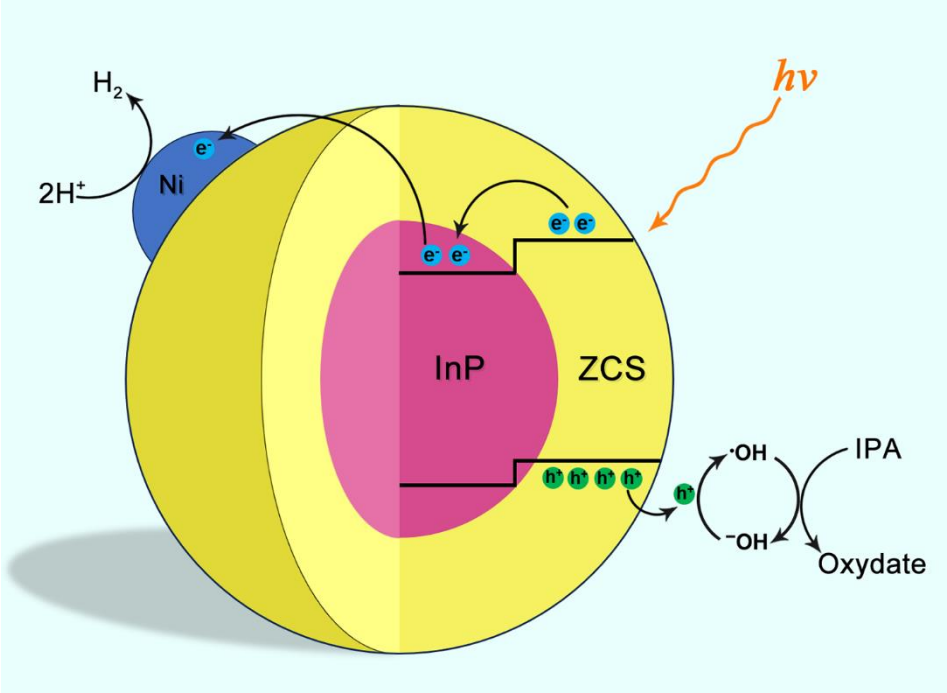

Figure 7. Schematic illustration of the mechanism of photocatalytic H_2 evolution by $Zn_{0.25}Cd_{0.75}S$ core/shell QDs.

4. CONCLUSION

In summary, by utilizing the $Zn_xCd_{1-x}S$ alloy as the shell material, the InP/$Zn_xCd_{1-x}S$ core/shell QDs with the reverse Type-II band alignment have been constructed by regulating the ratio of Cd/Zn. On one hand, the alloyed shell would passivate the surface defects of InP core. And the increased ratio of Cd/Zn could also reduce the interface strain and lattice mismatch between the core and shell, which inhibits the recombination of photogenerated excitons at defect sites and improves the stability of photocatalysts. On the other hand, the reverse Type-II band alignment of InP/$Zn_{0.25}Cd_{0.75}S$ QDs would realize the spatial separation of photogenerated electrons and holes, which further suppresses their backward recombination. Moreover, the holes are confined in the shell, which is convenient for the hole transfer to the surface of QDs and the subsequent

photocatalytic oxidation reaction, the rate-determining step in photocatalytic systems. Under the comprehensive effect of the above factors, the InP/$Zn_{0.25}Cd_{0.75}S$-3MLs core/shell QDs exhibit exceptional photocatalytic activity and stability, the H_2 evolution rate of 376.19 μmol h^{-1} mg^{-1} remains almost constant within 46 h irradiation. We expect that the construction of reverse Type-II core/shell QDs by regulating the composition of shell would provide a new strategy for the design of nano-heterostructure.

ASSOCIATED CONTENT

Supporting Information

XRD patterns of $Zn_xCd_{1-x}S$ QDs, TEM of InP/$Zn_xCd_{1-x}S$ and ZCS QDs, additional XPS survey data, the valence band XPS spectra of InP QDs and $Zn_xCd_{1-x}S$, UV-vis of InP QDs, $Zn_xCd_{1-x}S$ QDs and InP/ZCS-2MLs core/shell QDs, the PL of InP/ZCS with different shell thickness, the XRD patterns of InP/$Zn_{0.25}Cd_{0.75}S$-3MLs QDs before and after irradiation, long-time photocatalytic H_2 evolution of InP/CdS-3MLs, the electrochemical test of InP QDs and InP/ZCS with different shell thickness, EDS atomic composition of S, Zn and Cd in InP/ZCS-3MLs, ICP-MS atomic content of In, P, S, Zn and Cd in InP/ZCS-3MLs, compare with other photocatalytic systems, material characterization, calculation of lattice constant, apparent quantum yield of catalysts. (PDF)

AUTHOR INFORMATION

Corresponding Authors

Yu-ji Gao - School of Chemistry and Chemical Engineering, Faculty of Chemistry and Pharmacy, Qilu University of Technology (Shandong Academy of Science), Jinan 250353, Shandong, P. R. China; Email: yjgao@qlu.edu.cn

Authors

Dongzi Xu - School of Chemistry and Chemical Engineering, Faculty of Chemistry and Pharmacy, Qilu University of Technology (Shandong Academy of Science), Jinan 250353, Shandong, P. R. China.

Li-Lei Shen - School of Chemistry and Chemical Engineering, Faculty of Chemistry and Pharmacy, Qilu University of Technology (Shandong Academy of Science), Jinan 250353, Shandong, P. R. China.

Zhi-Kai Qin - School of Chemistry and Chemical Engineering, Faculty of Chemistry and Pharmacy, Qilu University of Technology (Shandong Academy of Science), Jinan 250353, Shandong, P. R. China.

Shuo Yan - School of Chemistry and Chemical Engineering, Faculty of Chemistry and Pharmacy, Qilu University of Technology (Shandong Academy of Science), Jinan 250353, Shandong, P. R. China.

Nianxing Wang - Department of Mechanical and Materials Engineering, University of Turku, Turku, 20014, Finland.

Jingui Wang - School of Chemistry and Chemical Engineering, Faculty of Chemistry and Pharmacy, Qilu University of Technology (Shandong Academy of Science), Jinan 250353, Shandong, P. R. China.

Notes

The authors declare no competing financial interest.

ACKONWLEDGMENTS

The authors are grateful for financial support from the National Natural Science Foundation of China (22002065, 52072190), Natural Science Foundation of Shandong Province (ZR2020QB060, ZR2020MB016).

RENFERENCE

(1) Wang, M.; Zhou, H.; Wang, F. Photocatalytic biomass conversion for hydrogen and renewable carbon-based chemicals. *Joule* **2024,** *8* (3), 604–621.

(2) Rahman, M. Z.; Edvinsson, T.; Gascon, J. Hole utilization in solar hydrogen production. *Nat. Rev. Chem.* **2022,** *6*, 243–258.

(3) Gao, Y.-J.; Li, X.-B.; Wang, X.-Z.; Zhao, N.-J.; Zhao, Y.; Wang, Y.; Xin, Z.-K.; Zhang, J.-P.; Zhang, T.; Tung, C.-H.; Wu, L.-Z. Site- and Spatial-Selective Integration of Non-noble Metal Ions into Quantum Dots for Robust Hydrogen Photogeneration. *Matter* **2020,** *3* (2), 571–585.

(4) Xiang, X.; Zhang, L.; Luo, C.; Zhang, J.; Cheng, B.; Liang, G.; Zhang, Z.; Yu, J. Ultrafast electron transfer from CdS quantum dots to atomically-dispersed Pt for enhanced H_2 evolution and value-added chemical synthesis. *Appl. Catal., B* **2024,** *340*, 123196.

(5) Long, H.; Gao, D.; Wang, P.; Wang, X.; Chen, F.; Yu, H. Amorphization-induced reverse electron transfer in NiB cocatalyst for boosting photocatalytic H_2 production. *Appl. Catal., B* **2024,** *340*, 123270.

(6) Bie, C.; Wang, L.; Yu, J. Challenges for photocatalytic overall water splitting. *Chem* **2022,** *8* (6), 1567–1574.

(7) Xu, J.; Zhang, X.; Yan, W.; Xie, T.; Chen, Y.; Wei, Y. Optimizing Electronic Density at Active W Sites for Boosting Photocatalytic H_2 Evolution. *Inorg. Chem.* **2024,** *63* (9), 4279–4287.

(8) Zhu, Y.; Ren, J.; Huang, G.; Dong, C.-L.; Huang, Y.-C.; Lu, P.; Tang, H.; Liu, Y.; Shen, S.; Yang, D. Red Phosphorus Grafted High-Index (116) Faceted Anatase TiO_2 for Z-Scheme Photocatalytic Pure Water Splitting. *Adv. Funct. Mater.* **2024,** *34* (9), 2311623.

(9) Wang, X.; An, C.; Zhang, S.; Wang, S.; Li, J.; Zhu, Y. Metal-free heterostructured 2D/1D polymeric carbon nitride/fibrous phosphorus for boosted photocatalytic hydrogen production from pure water. *Sep. Purif. Technol.* **2024,** *340*, 126733.

(10) Wang, K.; Tao, Y.; Tang, Z.; Xu, X.; Benetti, D.; Vidal, F.; Zhao, H.; Rosei, F.; Sun, X. Efficient Photoelectrochemical Hydrogen Generation Based on Core Size Effect of Heterostructured Quantum Dots. *Small* **2023**, 2306453.

(11) Su, H.; Wang, W.; Shi, R.; Tang, H.; Sun, L.; Wang, L.; Liu, Q.; Zhang, T. Recent advances in quantum dot catalysts for hydrogen evolution: Synthesis, characterization, and photocatalytic application. *Carbon Energy* **2023,** *5* (9), e280.

(12) Yan, Y.; Crisp, R. W.; Gu, J.; Chernomordik, B. D.; Pach, G. F.; Marshall, Ashley R.; Turner, J. A.; Beard, M. C. Multiple exciton generation for photoelectrochemical hydrogen evolution reactions with quantum yields exceeding 100%. *Nat. Energy* **2017,** *2* (5), 17052.

(13) Kong, L.; Ji, Y.; Dang, Z.; Yan, J.; Li, P.; Li, Y.; Liu, S. g-C_3N_4 Loading Black Phosphorus Quantum Dot for Efficient and Stable Photocatalytic H_2 Generation under Visible Light. *Adv. Funct. Mater.* **2018,** *28* (22), 1800668.

(14) Zeng, S.; Tan, W.; Si, J.; Mao, L.; Shi, J.; Li, Y.; Hou, X. Ultrafast Electron Transfer in InP/ZnSe/ZnS Quantum Dots for Photocatalytic Hydrogen Evolution. *J. Phys. Chem. Lett.* **2022,** *13* (39), 9096–9102.

(15) Liu, J.; Yue, S.; Zhang, H.; Wang, C.; Barba, D.; Vidal, F.; Sun, S.; Wang, Z. M.; Bao, J.; Zhao, H.; Selopal, G. S.; Rosei, F. Efficient Photoelectrochemical Hydrogen Generation Using Eco-Friendly “Giant” InP/ZnSe Core/Shell Quantum Dots. *ACS Appl. Mater. Interfaces* **2023,** *15* (29), 34797–34808.

(16) Jalali, H. B.; Sadeghi, S.; Dogru Yuksel, I. B.; Onal, A.; Nizamoglu, S. Past, present and future of indium phosphide quantum dots. *Nano Res.* **2022,** *15* (5), 4468–4489.

(17) Cui, Z.; Mei, S.; Wen, Z.; Yang, D.; Qin, S.; Xiong, Z.; Yang, B.; He, H.; Bao, R.; Qiu, Y.; Chen, Y.; Zhang, W.; Xie, F.; Xing, G.; Guo, R. Synergistic Effect of Halogen Ions and Shelling Temperature on Anion Exchange Induced Interfacial Restructuring for Highly Efficient Blue Emissive InP/ZnS Quantum Dots. *Small* **2022,** *18* (15), 2108120.

(18) Reiss, P.; Protiere, M.; Li, L. Core/Shell semiconductor nanocrystals. *Small* **2009,** *5* (2), 154–168.

(19) Haubold, S.; Haase, M.; Kornowski, A.; Weller, H. Strongly Luminescent InP/ZnS Core-Shell Nanoparticles. *ChemPhysChem* **2001,** *2*, 331–334.

(20) Panzer, R.; Guhrenz, C.; Haubold, D.; Hübner, R.; Gaponik, N.; Eychmüller, A.; Weigand, J. J. Versatile Tri(pyrazolyl)phosphanes as Phosphorus Precursors for the Synthesis of Highly Emitting InP/ZnS Quantum Dots. *Angew. Chem. Int. Ed.* **2017,** *56* (46), 14737–14742.

(21) Yu, S.; Fan, X. B.; Wang, X.; Li, J.; Zhang, Q.; Xia, A.; Wei, S.; Wu, L. Z.; Zhou, Y.; Patzke, G. R. Efficient photocatalytic hydrogen evolution with ligand engineered all-inorganic InP and InP/ZnS colloidal quantum dots. *Nat. Commun.* **2018,** *9* (1), 4009.

(22) Bang, J.; Das, S.; Yu, E. J.; Kim, K.; Lim, H.; Kim, S.; Hong, J. W. Controlled Photoinduced Electron Transfer from InP/ZnS Quantum Dots through Cu Doping: A New Prototype for the Visible-Light Photocatalytic Hydrogen Evolution Reaction. *Nano Lett.* **2020,** *20* (9), 6263–6271.

(23) Zhang, W.; Ding, S.; Zhuang, W.; Wu, D.; Liu, P.; Qu, X.; Liu, H.; Yang, H.; Wu, Z.; Wang, K.; Sun, X. W. InP/ZnS/ZnS Core/Shell Blue Quantum Dots for Efficient Light‐Emitting Diodes. *Adv. Funct. Mater.* **2020,** *30* (49), 2005303.

(24) Cao, F.; Wang, S.; Wang, F.; Wu, Q.; Zhao, D.; Yang, X. A Layer-by-Layer Growth Strategy for Large-Size InP/ZnSe/ZnS Core–Shell Quantum Dots Enabling High-Efficiency Light-Emitting Diodes. *Chem. Mater.* **2018,** *30* (21), 8002–8007.

(25) Lim, J.; Bae, W. K.; Lee, D.; Nam, M. K.; Jung, J.; Lee, C.; Char, K.; Lee, S. InP@ZnSeS, Core@Composition Gradient Shell Quantum Dots with Enhanced Stability. *Chem. Mater.* **2011,** *23* (20), 4459–4463.

(26) Lim, J.; Park, M.; Bae, W. K.; Lee, D.; Lee, S.; Lee, C.; Char, K. Highly Efficient Cadmium-Free Quantum Dot Light-Emitting Diodes Enabled by the Direct Formation of Excitons within InP@ZnSeS Quantum Dots. *ACS Nano* **2013,** *7*, 9019–9026.

(27) Omogo, B.; Gao, F.; Bajwa, P.; Kaneko, M.; Heyes, C. D. Reducing Blinking in Small Core-Multishell Quantum Dots by Carefully Balancing Confinement Potential and Induced Lattice Strain: The “Goldilocks” Effect. *ACS Nano* **2016,** *10* (4), 4072–4082.

(28) Rafipoor, M.; Dupont, D.; Tornatzky, H.; Tessier, M. D.; Maultzsch, J.; Hens, Z.; Lange, H. Strain Engineering in InP/(Zn,Cd)Se Core/Shell Quantum Dots. *Chem. Mater.* **2018,** *30* (13), 4393–4400.

(29) Pietra, F.; De Trizio, L.; Hoekstra, A. W.; Renaud, N.; Prato, M.; Grozema, F. C.; Baesjou, P. J.; Koole, R.; Manna, L.; Houtepen, A. J. Tuning the Lattice Parameter of In_xZn_yP for Highly Luminescent Lattice-Matched Core/Shell Quantum Dots. *ACS Nano* **2016,** *10* (4), 4754–4762.

(30) Dupont, D.; Tessier, M. D.; Smet, P. F.; Hens, Z. Indium Phosphide-Based Quantum Dots with Shell-Enhanced Absorption for Luminescent Down-Conversion. *Adv. Mater.* **2017,** *29* (29), 1700686.

(31) Zhu, H.; Song, N.; Lian, T. Controlling Charge Separation and Recombination Rates in CdSe/ZnS Type I Core-Shell Quantum Dots by Shell Thicknesses. *J. Am. Chem. Soc.* **2010,** *132* (42), 15038–15045.

(32) Khan, S. U.; Eren, G. O.; Atac, N.; Onal, A.; Qureshi, M. H.; Cooper, F. K.; Almammadov, T.; Kolemen, S.; Sahin, M.; Can, F.; Nizamoglu, S. Antibacterial type-II InP/ZnO quantum dots via multimodal reactive oxygen species. *Chem. Eng. J.* **2024,** *480*, 148140.

(33) Wu, H. L.; Li, X. B.; Tung, C. H.; Wu, L. Z. Recent Advances in Sensitized Photocathodes: From Molecular Dyes to Semiconducting Quantum Dots. *Adv. Sci.* **2018,** *5* (4), 1700684.

(34) Sahu, A.; Kumar, D. Core-shell quantum dots: A review on classification, materials, application, and theoretical modeling. *J. Alloy. Compd.* **2022,** *924*, 166508.

(35) Sun, M.; Yan, T.; Yan, Q.; Liu, H.; Yan, L.; Zhang, Y.; Du, B. Novel visible-light driven g-C_3N_4/$Zn_{0.25}Cd_{0.75}S$ composite photocatalyst for efficient degradation of dyes and reduction of Cr(VI) in water. *RSC Adv.* **2014,** *4* (38), 19980–19986.

(36) Wang, L.; Zan, L. Band-gap-energy-adjustable and noble-metal-free modified NiS-$Zn_xCd_{1-x}S$ for highly efficient visible-light-driven Cr^{6+} photoreduction in alkaline wastewater. *J. Phys. Chem. Solids* **2021,** *150*, 109893.

(37) Cao, X.; Zhang, L.; Guo, C.; Wang, M.; Guo, J.; Wang, J. Construction of Zn_xCd_yS with a 3D Hierarchical Structure for Enhanced Photocatalytic Hydrogen Production from Water Splitting. *Inorg. Chem.* **2023,** *62* (46), 18990–18998.

(38) Qi, S.; Miao, Y.; Chen, J.; Chu, H.; Tian, B.; Wu, B.; Li, Y.; Xin, B. Controlled Biosynthesis of ZnCdS Quantum Dots with Visible-Light-Driven Photocatalytic Hydrogen Production Activity. *Nanomaterials* **2021,** *11* (6), 1357.

(39) Toufanian, R.; Piryatinski, A.; Mahler, A. H.; Iyer, R.; Hollingsworth, J. A.; Dennis, A. M. Bandgap Engineering of Indium Phosphide-Based Core/Shell Heterostructures Through Shell Composition and Thickness. *Front. Chem.* **2018,** *6*, 567.

(40) Gao, R.; Cheng, B.; Fan, J.; Yu, J.; Ho, W. $Zn_xCd_{1-x}S$ quantum dot with enhanced photocatalytic H_2-production performance. *Chin. J. Catal.* **2021,** *42* (1), 15–24.

(41) Wang, Z.; Wang, L.; Cheng, B.; Yu, H.; Yu, J. Photocatalytic H_2 Evolution Coupled with Furfuralcohol Oxidation over Pt‐Modified ZnCdS Solid Solution. *Small Methods* **2021,** *5* (11), 2100919.

(42) Xiao, Q.; Yang, T.; Guo, X.; Jin, Z. S-scheme heterojunction constructed by ZnCdS and $CoWO_4$ nano-ions promotes photocatalytic hydrogen production. *Surf. Interfaces* **2023,** *43*, 103577.

(43) Zhao, J.; Chen, X.; Chen, B.; Luo, X.; Sun, T.; Zhang, W.; Wang, C.; Lin, J.; Su, D.; Qiao, X.; Wang, F. Accurate Control of Core-Shell Upconversion Nanoparticles through Anisotropic Strain Engineering. *Adv. Funct. Mater.* **2019,** *29* (44), 1903295.

(44) Dennis, A. M.; Mangum, B. D.; Piryatinski, A.; Park, Y. S.; Hannah, D. C.; Casson, J. L.; Williams, D. J.; Schaller, R. D.; Htoon, H.; Hollingsworth, J. A. Suppressed blinking and auger recombination in near-infrared type-II InP/CdS nanocrystal quantum dots. *Nano Lett.* **2012,** *12* (11), 5545–5551.

(45) Virieux, H.; Le Troedec, M.; Cros-Gagneux, A.; Ojo, W.-S.; Delpech, F.; Nayral, C.; Martinez, H.; Chaudret, B. InP/ZnS Nanocrystals: Coupling NMR and XPS for Fine Surface and Interface Description. *J. Am. Chem. Soc.* **2012,** *134* (48), 19701–19708.

(46) Smith, C. T.; Leontiadou, M. A.; Clark, P. C. J.; Lydon, C.; Savjani, N.; Spencer, B. F.; Flavell, W. R.; O'Brien, P.; Binks, D. J. Multiple Exciton Generation and Dynamics in InP/CdS Colloidal Quantum Dots. *J. Phys. Chem. C* **2017,** *121* (4), 2099–2107.

(47) Xie, Q.; Wang, M.; Xu, Y.; Li, X.; Zhou, X.; Hong, L.; Jiang, L.; Lin, W.-F. S vacancy modulated $Zn_xCd_{1-x}S$/CoP quantum dots for efficient H_2 evolution from water splitting under visible light. *J. Energy Chem.* **2021,** *61*, 210–218.

(48) Yu, T.; Si, Y.; Lv, Z.; Wang, K.; Zhang, Q.; Liu, X.; Wang, G.; Xie, G.; Jiang, L. $Cd_{0.5}Zn_{0.5}S/Ni_2P$ noble-metal-free photocatalyst for high-efficient photocatalytic hydrogen production: Ni_2P boosting separation of photocarriers. *Int. J. Hydrogen Energy* **2019,** *44* (60), 31832–31840.

(49) Qin, Z.; Xue, F.; Chen, Y.; Shen, S.; Guo, L. Spatial charge separation of one-dimensional Ni_2P-$Cd_{0.9}Zn_{0.1}S$/g-C_3N_4 heterostructure for high-quantum-yield photocatalytic hydrogen production. *Appl. Catal., B* **2017,** *217*, 551–559.

(50) Tessier, M. D.; Dupont, D.; De Nolf, K.; De Roo, J.; Hens, Z. Economic and Size-Tunable Synthesis of InP/ZnE (E = S, Se) Colloidal Quantum Dots. *Chem. Mater.* **2015,** *27* (13), 4893–4898.

(51) Chu, L.; Zhang, J.; Xiang, H.; Wu, S.; Jia, Y.; Liu, C. Synergetic Effects of Zn Alloying and Defect Engineering on Improving the CdS Buffer Layer of Cu_2ZnSnS_4 Solar Cells. *Inorg. Chem.* **2022,** *61* (31), 12293–12300.

(52) Deng, Z.; Lie, F. L.; Shen, S.; Ghosh, I.; Mansuripur, M.; Muscat, A. J. Water-Based Route to Ligand-Selective Synthesis of ZnSe and Cd-Doped ZnSe Quantum Dots with Tunable Ultraviolet A to Blue Photoluminescence. *Langmuir* **2009,** *25* (1), 434–442.

(53) Zhu, Y.; Jin, T.; Lian, T.; Egap, E. Enhancing the efficiency of semiconducting quantum dot photocatalyzed atom transfer radical polymerization by ligand shell engineering. *J. Chem. Phys.* **2021,** *154* (20), 204903.

(54) Li, X.-B.; Li, Z.-J.; Gao, Y.-J.; Meng, Q.-Y.; Yu, S.; Weiss, R. G.; Tung, C.-H.; Wu, L.-Z. Mechanistic Insights into the Interface-Directed Transformation of Thiols into Disulfides and Molecular Hydrogen by Visible-Light Irradiation of Quantum Dots. *Angew. Chem. Int. Ed.* **2014,** *53* (8), 2085–2089.

(55) Simon, T.; Bouchonville, N.; Berr, M. J.; Vaneski, A.; Adrović, A.; Volbers, D.; Wyrwich, R.; Döblinger, M.; Susha, A. S.; Rogach, A. L.; Jäckel, F.; Stolarczyk, J. K.; Feldmann, J. Redox shuttle mechanism enhances photocatalytic H_2 generation on Ni-decorated CdS nanorods. *Nat. Mater.* **2014,** *13* (11), 1013–1018.

(56) Zhong, W.; Huang, X.; Xu, Y.; Yu, H. One-step facile synthesis and high H_2-evolution activity of suspensible $Cd_xZn_{1-x}S$ nanocrystal photocatalysts in a S^{2-}/SO^{2-} system. *Nanoscale* **2018,** *10* (41), 19418–19426.

(57) Gao, Y.-J.; Li, X.-B.; Wu, H.-L.; Meng, S.-L.; Fan, X.-B.; Huang, M.-Y.; Guo, Q.; Tung, C.-H.; Wu, L.-Z. Exceptional Catalytic Nature of Quantum Dots for Photocatalytic Hydrogen Evolution without External Cocatalysts. *Adv. Funct. Mater.* **2018,** *28* (33), 1801769.

(58) Do, K. H.; Kumar, D. P.; Rangappa, A. P.; Hong, Y.; Reddy, D. A.; Kim, T. K. Indium Phosphide Quantum Dots Integrated with Cadmium Sulfide Nanorods for Photocatalytic Carbon Dioxide Reduction. *ChemCatChem* **2020,** *12* (18), 4550–4557.

(59) Wu, K.; Chen, Z.; Lv, H.; Zhu, H.; Hill, C. L.; Lian, T. Hole Removal Rate Limits Photodriven H_2 Generation Efficiency in CdS-Pt and CdSe/CdS-Pt Semiconductor Nanorod–Metal Tip Heterostructures. *J. Am. Chem. Soc.* **2014,** *136* (21), 7708–7716.

Table of Contents

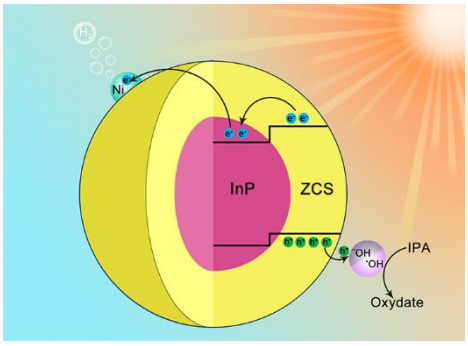

The reverse Type-II InP/$Zn_xCd_{1-x}S$ Core/shell QDs have been well designed to realize exceptional photocatalytic H_2 evolution.